RSC Advances

PAPER

View Article Online
View Journal | View Issue

Cite this: *RSC Adv.*, 2025, **15**, 43322

A disposable, passive microfluidic cartridge for point-of-care detection of antibodies in total capillary blood based on hemagglutination and machine-learning assisted interpretation

Munawar Jawad, *[a] Afroza Tabassum Akhi,[a] Rian Wendling,[b] Vanessa Redecke,[bc] Hans Häcker[bc] and Bruce Gale [a]

Point-of-care (PoC) detection of antibodies in blood enables rapid, on-site diagnosis. However, these devices often face challenges related to user variability due to the requirement of multiple manual operations. To address this issue, we designed and developed a disposable microfluidic device that requires minimal user input for rapid detection of SARS-CoV-2 antibodies (ABs) in total blood and antigens associated with blood types. Here, we present a passive pressure-driven pumping technique that rapidly mixes blood samples with reagents, delivering results within three minutes. The device requires 15 μL of capillary blood and can detect SARS-CoV-2 ABs across a concentration range of 0 to 60 μg mL^{-1}. Additionally, we demonstrated the versatility of the microfluidic device by implementing blood typing functionality, highlighting its potential for broader serological testing applications. We also developed a support vector machine (SVM) algorithm as a proof-of-concept to demonstrate the potential application of machine learning (ML)-based analysis to complement visual interpretation of results. We evaluated the performance and predictive accuracy of the SVM model and compared it to human interpretations. The analysis showed that the SVM model achieved a statistically significant improvement in predicting varying degrees of agglutination when compared to human interpretation. This device addresses the need for a user-friendly, rapid COVID-19 AB testing solution and blood-typing assay and also provides a model for the future development of diagnostic devices that are integrated with ML models for improved diagnostic accuracy and accessibility in both clinical and non-clinical environments.

Received 5th August 2025
Accepted 26th October 2025

DOI: 10.1039/d5ra05719a

rsc.li/rsc-advances

1. Introduction

The outbreak of COVID-19 has shown that diagnostic tests are indispensable tools to manage pandemic situations. Serological assays, designed to detect the presence of specific antibodies (ABs) against designated antigens, are pivotal in the management and understanding of the COVID-19 pandemic and other diseases. When dealing with infectious diseases, these assays facilitate the identification of individuals who have been exposed to the virus, contributing to epidemiological studies and the development of strategies for disease control and prevention. Several tests are available for detecting the presence of ABs against SARS-CoV-2, including the enzyme-linked immunosorbent assays (ELISA), chemiluminescence immunoassays (CLIA), neutralization assays (NA), and lateral flow immunoassays (LFIA). Although lab-based techniques like ELISA, CLIA, and NA have high sensitivity and specificity, they require complex instruments as well as a long turnaround time. These techniques are also typically costly.[1–3] Point-of-care (PoC) devices address many of these limitations due to their simplicity, fast sample-to-result time, and cost-effectiveness.[4,5] Lateral flow immunoassay (LFIA) is a commonly used point-of-care test that can detect AB presence in a blood sample and provide qualitative results. While these tests can be conducted without requiring sophisticated equipment and expert knowledge, the sensitivity of LFIA is worse than the standards achieved in laboratory-conducted tests.[6,7] Another AB detection technique used in point-of-care settings is the hemagglutination test (HAT), a technique in which red blood cells (RBCs) aggregate in the presence of viruses or antibodies. Typically, RBCs act as the source of antigens and interact with the glycoproteins on the viral surface or the antibodies, leading to the clumping of RBCs.[8–11] Owing to their inherent simplicity, cost-

[a]*Department of Mechanical Engineering, The University of Utah, Salt Lake City, UT 84112, USA. E-mail: munawar.jawad@utah.edu*

[b]*NanoSpot.ai, Salt Lake City, UT 84108, USA*

[c]*Division of Microbiology & Immunology, Department of Pathology, The University of Utah, Salt Lake City, UT 84112, USA*

effectiveness, and visual interpretability, hemagglutination assays are of particular interest to researchers.[12]

Despite their potential, significant challenges arise when using hemagglutination tests for point-of-care testing. First, recently developed PoC devices still involve complex setups and are not fully suited to be applied in PoC settings due to their high costs. In a recent study, Qu *et al.* developed a microflow cytometry-based agglutination immunoassay (MCIA) for point-of-care quantitative detection of SARS-CoV-2 IgM and IgG antibodies.[13] The MCIA technique offers advantages such as a low limit of detection, a small volume of sample consumption (10 μL), and a compact setup. However, their developed method requires expert knowledge to perform the assay and takes about 30 minutes. Another HAT study introduces a portable lens-free imaging system coupled with a particle agglutination assay as a biosensor for SARS-CoV-2, enabling accurate detection of the virus in complex samples.[14] The proposed biosensor combines computational imaging and deep learning to image and quantify individual microbeads undergoing agglutination, allowing for the detection of SARS-CoV-2 levels. Nevertheless, the usage of integrated electronics (LED arrays and specific optical filters) comes with high manufacturing cost and complexity, which does not make the device fabrication process suitable for mass production. Second, user variability due to the nature of the operations of some devices can lead to inconsistent test results. For example, a couple of studies have developed card-based at-home COVID-19 tests.[15,16] These tests offer the advantage of HAT's simplicity and user-friendliness. Both studies developed a highly sensitive hemagglutination-based semi-quantitative assay for detecting SARS-CoV-2 ABs. However, these tests require that users themselves mix the blood sample with the reagent and tilt the card, which can lead to inconsistent results due to variations in how individuals perform the actions. Therefore, even though card-based assays are suitable for home testing, the need for manual mixing and tilting leads to variability that can negatively affect the performance of the assays.

We identified that integrating a single passive method for both pumping and mixing into at-home tests can mitigate user variability. In principle, the developed passive technique should fulfill several criteria: it should be simple to perform, able to pump low-volume fluids autonomously, and mix them efficiently and swiftly. Many studies have explored a variety of passive pumping techniques, such as capillary pumping,[17] surface-tension-driven flow,[18] gravity-driven flow,[19] osmotic flow,[20] and finger-powered flow.[21] However, each of the techniques has its own limitations. For example, since the Reynolds number (Re) is low in capillary flow, it is not suitable for the fast mixing of two fluids. Moreover, surface-tension-driven flow and gravity-driven flow require a consistent supply of solutions to maintain continuous flow, meaning they are not suitable for low-volume applications.[22,23] Osmotic flow, on the other hand, requires a more complicated setup than the techniques mentioned above.[24] Lastly, finger-powered flow is vulnerable to inconsistencies since finger pressure can vary from person to person.[23,25] No existing pumping technique meets the criteria necessary to address the problem of user variability.

To overcome the limitations of existing pumping techniques, we developed a pressure-driven pumping mechanism that develops pressure when the assay well caps are closed and that can be released to accomplish passive mixing of a blood sample and reagent. Since the caps always lock at the same position when snapped, the variability from user to user is minimal with this method. We also designed and fabricated a disposable microfluidic cartridge to be used in point-of-care HAT assays, which we successfully implemented for the detection of SARS-CoV-2 ABs in blood. The chip is designed to perform rapid mixing of RBCs and proteins, requiring only 3 minutes from sample to result, which is 3 to 5 times faster compared to available LFIA-based PoC tests. Furthermore, we chose materials that are inexpensive, do not require complex processing for device fabrication, and are applicable for roll-to-roll manufacturing, making the fabrication process suitable for mass production. Finally, we developed a proof-of-concept analysis method using a machine learning algorithm, which overcomes some of the variations caused by the subjective nature of visual readout. Our developed code demonstrates how this study can be integrated with artificial intelligence (AI)-based platforms to obtain accurate interpretation. With the quick turnaround time, cost-effective materials, and scalability for mass production, our developed "drop-and-forget" microfluidic chip holds promise for accessible and efficient point-of-care diagnostics for a variety of diseases.

2 Materials and methods

2.1 Device materials, clinical sample, and reagent

The device consists of two polyester films, 3M™ 9960 and 3M™ 9972A. Both materials are approved by 3M's Medical Materials Technology division for use in healthcare medical devices. 3M 9960 is a transparent polyester film with a hydrophilic coating on both sides. 3M 9972A, used as the fluid layer, is a white polyester film coated with hydrophobic double-sided acrylate adhesive. 0.2 mL centrifuge tubes were purchased from Stellar Scientific Ltd. Polydimethylsiloxane (PDMS) was purchased from Ellsworth Adhesives. The pressure-sensitive adhesive (3M Scotchcal™ 220) was sourced from Graphic Marking Systems Media. Whole blood samples were collected from the blood bank (ARUP Blood Services). The reagents for both the SARS-CoV-2 total antibody test and the blood grouping test were provided by Nanospot.ai. For the SARS-CoV-2 antibody test, the reagent comprises a recombinant fusion protein with a high-affinity binding domain for RBCs and the Spike-RBD protein, which acts as the antigen for antibodies specific to SARS-CoV-2. Additional details on the design of the recombinant protein can be found here.[16] The blood grouping reagents include off-the-shelf anti-A, anti-B, and anti-D antibodies, which detect the presence of A, B, and RhD antigens, respectively.

2.2 Design rationale

To implement the assay, we needed a design that could facilitate fast mixing and did not require a large sample volume. After some review and testing, we based our design on serpentine

channels that generate moderate Dean flow for mixing while being simple to fabricate and relatively small. Since blood is more viscous than the reagent, it experiences greater drag, slowing the flow. To minimize the blood sample's flow resistance and energy loss, we designed the blood-sample inlet (inlet 1) to be on the same plane as the serpentine channels. The length of each inlet connecting to the small chamber has also been carefully designed so that the reagent enters the small chamber before the blood when both fluids are pressurized due to the cap-closure of the centrifuge tubes. This chamber plays a vital role as it initiates the mixing between the fluids. When the caps are closed together, 1.2 μL (same as the chamber volume) of blood and reagent enter the chamber and get mixed. The fluid then moves evenly from the chamber and inlets, facilitating complete mixing as the fluids move forward.

Design features such as the channel geometry and number of serpentine units are critical considerations to achieve effective mixing. Design parameters such as the length and width of the serpentine units were explored and optimized empirically. We investigated three different lengths of the serpentine channels: 1 mm, 5 mm, and 10 mm. As expected, 10 mm provided the best mixing since it facilitated more diffusion of the fluids compared to the smaller lengths. Also, we observed that agglutinated sample distribution can be better visualized in the 10 mm long channels, which is convenient for both users and the machine learning tool for interpreting the results.

Moreover, we tested different widths, such as 200, 300, 400, and 500 μm, for the channels. We observed that anything below 400 μm results in channel blockage when the samples agglutinate. We selected 400 μm to reduce both the dead volume and the volume required for the sample and reagent.

The design incorporates two chambers after the mixing zone, a small chamber having a 4 mm diameter, followed by an 8 mm diameter chamber. The purpose of the 4 mm chamber is to help the fluid achieve a specific flow rate. We tested two different shapes (diamond and circular) for this chamber. For channels with the geometry specified above, we could not achieve the flow rate required to sufficiently mix blood samples and reagents in the diamond-shaped chamber. We also varied the diameter of this chamber from 2 mm to 8 mm. We observed that the critical flow rate required for the operation of the device is achieved when the smaller chamber is half the diameter of the bigger chamber. The bigger 8 mm chamber acts as a reservoir and holds the blood-reagent mixture inside the device.

2.3 Fabrication

The device is designed to perform passive pumping and mixing of the blood sample and the reagent. The blood sample and the reagent are introduced *via* inlets into serpentine channels, where they flow and mix passively due to the pressure generated from cap closure. The design also includes two chambers at the end of the serpentine channels to help achieve the desired flow rate and hold the blood-reagent mixture inside the device as a safety precaution. The fabrication steps of the microfluidic device are shown in Fig. 1. The design was made in AutoCAD (Autodesk, Inc), and all three layers were cut through using a CO_2 laser (VLS 3.75, Universal Laser Systems Inc). All three layers were cut using the same laser parameters: 10% power, 8% speed, 1000 PPI and single pass. The white fluidic layer (3M 9972A) with adhesive on both sides was manually sandwiched between two 3M 9960 films from the top and bottom at room temperature. Then, PDMS ports (punched through, 4 mm diameter opening) were attached *via* plasma bonding (Dyne-A-Mite™, Enercon Industries Corporation) on top of the inlets to hold the centrifuge tubes. To hold blood samples and reagent, we used 0.2 mL centrifuge tubes. The tubes were cut to have 2.5 mm openings at the bottom, facilitating connections to the channels. Table 1 presents the list of the materials with dimensions and costs of the chip components.

2.4 Hemagglutination assay

We implemented hemagglutination assays for SARS-CoV-2 AB detection and blood group identification in blood samples. To detect the SARS-CoV-2 ABs in user blood, we used a hemagglutination assay developed by Redecke *et al.*, where they developed a recombinant protein named Nanospike that binds with the ABs on the RBC's surface, resulting in visible agglutination.[16] The construction of the recombinant protein and the assay principle is presented in Fig. 2a and b. When total blood is mixed with the reagent, the bispecific protein attaches to the RBCs. If spike-antibodies are present in the blood, they bind to the Spike-RBD, resulting in visible hemagglutination of the RBCs. No hemagglutination occurs if the spike antibodies are absent. We performed blood grouping hemagglutination tests on AB+ and O+ patient blood samples, using anti-A, anti-B, and anti-D antibody reagents (Fig. 2c).

2.5 Working principle

Fig. 3 provides an overview of the whole on-chip testing procedure. For testing, users will need to perform a fingerstick and collect 15 μL of blood using a plastic capillary. They will then load 15 μL of the fresh blood sample and 15 μL of the reagent into the designated tubes of the microchip. For the experiments, we used pipettes instead of capillaries to load the whole blood sample (no more than two days old) and the reagent as the first step of the assay. Once the blood sample and reagent are loaded inside the tubes in separate inlets, a pressure-sensitive adhesive (PSA) is placed on top of the vent to seal the air inside the device. As both caps are closed together after the loading phase, the air inside the tubes induces pressure on the fluid surfaces. However, the fluids cannot flow at this point, even after being pressurized, since the air has been trapped by the PSA, preventing a pressure gradient. The vent is opened to atmospheric pressure as the PSA is removed, and a pressure gradient is generated that flows both fluids evenly and simultaneously from the inlets. As the fluids flow together through the serpentine units, the RBCs interact with the reagent and initiate the agglutination reaction. The agglutinated sample can be observed within 3 minutes. For instantaneous interpretation of the test result, the user can compare the agglutinated sample with control images. For a more quantitative interpretation, the

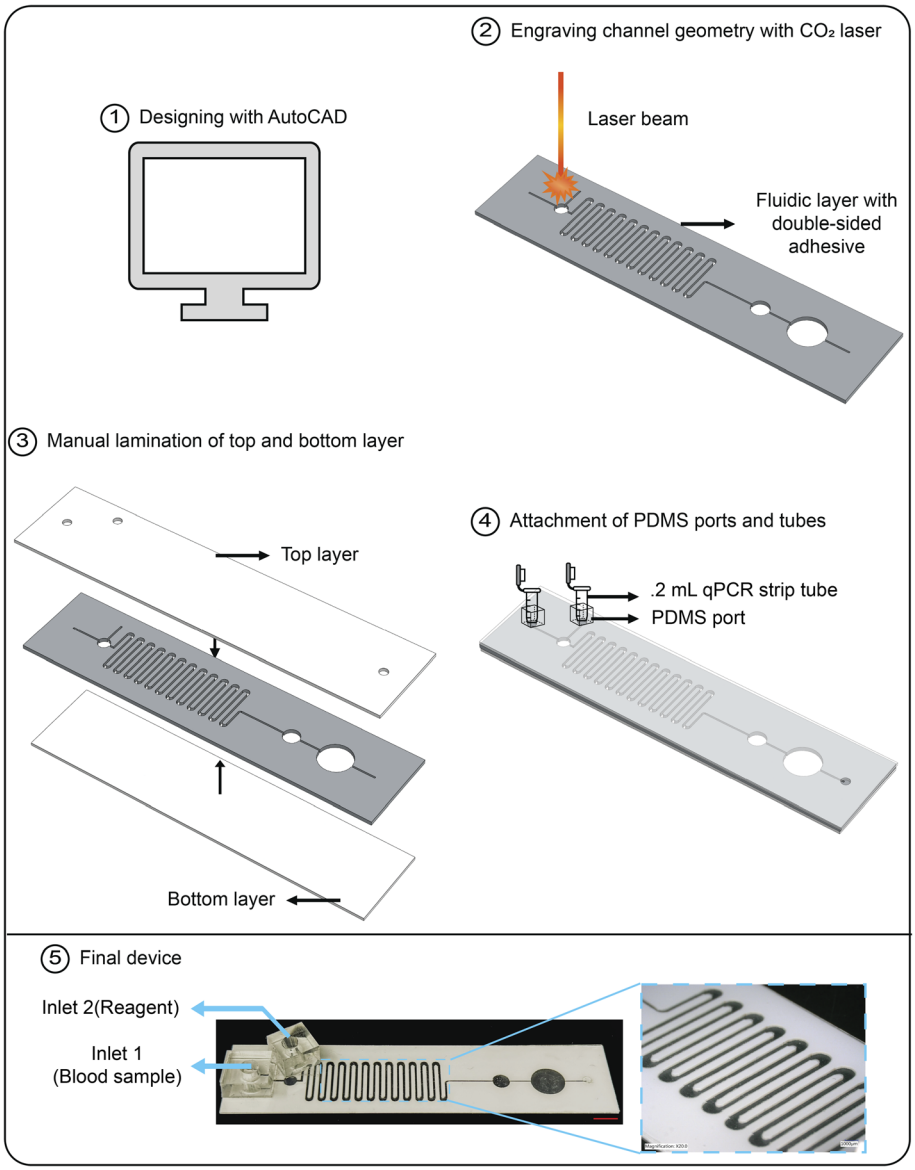

Fig. 1 Fabrication process of the microfluidic device. (1) The process begins with designing device geometry in AutoCAD software. The design defines the dimensions and layout of fluidic channels and other features. (2) Using a CO_2 laser, the channel geometry is engraved onto a fluidic layer consisting of a double-sided tape. Similarly, the top and the bottom layers are cut using the laser with appropriate features and dimensions. (3) After engraving, the top and bottom layers of the device are laminated manually to enclose the channels, forming a complete, sealed microfluidic structure. (4) PDMS ports and 0.2 mL tubes are attached to the inlets for fluidic interfacing. The tubes are cut to have a 2.5 mm opening at the bottom to facilitate fluid entrance. (5) The final assembled device displays the completed serpentine microfluidic channel structure (Scale bar in red = 2 mm). The inset highlights the intricate details of the serpentine channels, confirming successful fabrication of the designed geometry.

Table 1 Estimated material costs per microfluidic device

Chip component	Dimension	Amount (Ct.)	Cost (USD)
3M 9972A	99 (L) × 21 (W) × 0.21 (H) mm^3	1	$0.03
3M 9960	99 (L) × 21 (W) × 0.175 (H) mm^3	2	$0.04
PDMS	10 (L) × 10 (W) × 5 (H) mm^3	2	$0.20
0.2 mL centrifuge tubes	22.2 mm (H) × 6.9 mm (OD)	2	$0.12
Scotchcal 220	30 (L) × 17 (W) × 0.063 (H) mm^3	1	$0.01
		Total cost =	$0.40

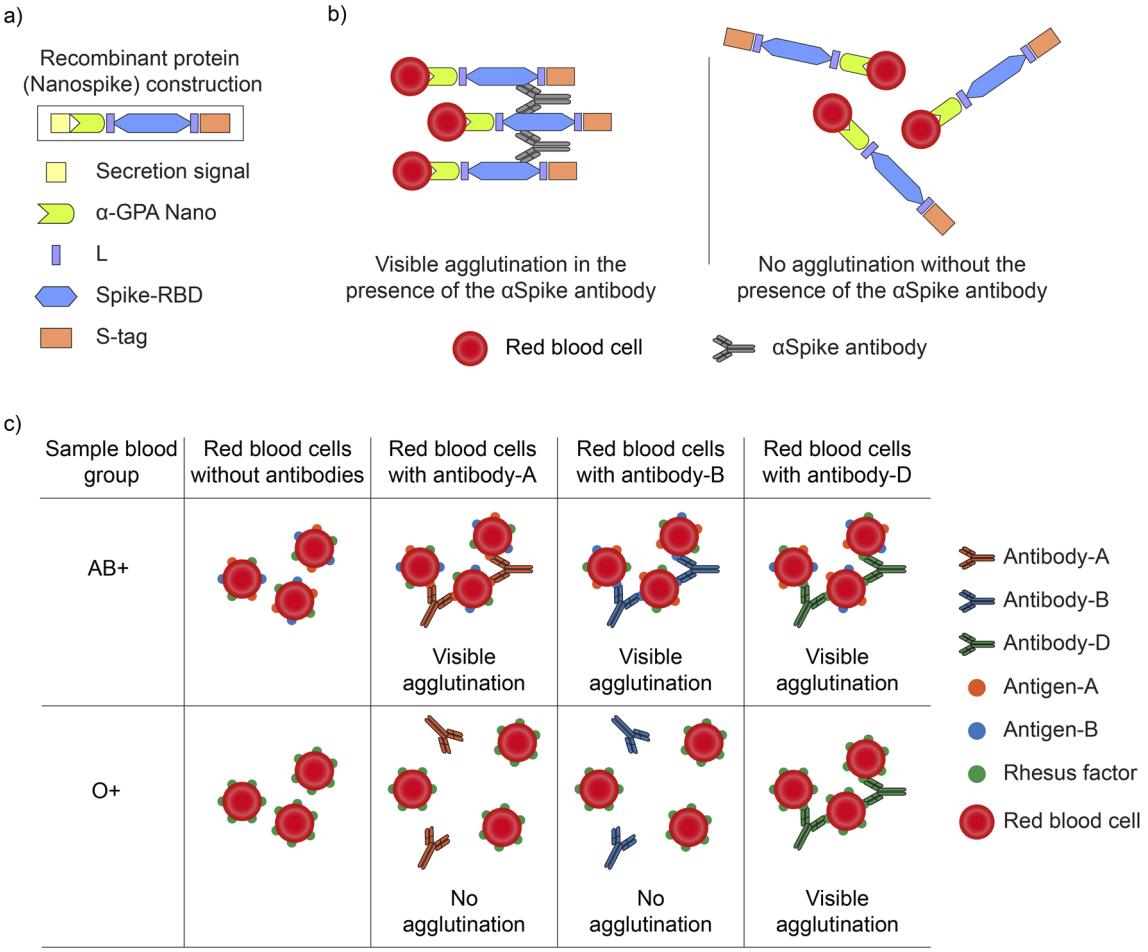

Fig. 2 Fusion protein construction and hemagglutination assay principle. (a) The bispecific protein consists of a nanobody directed against glycophorin A (GPA) expressed at high levels on RBCs and the receptor binding domain of the spike protein (Spike-RBD). (b) The nanobody mediates rapid binding to the red blood cells while the antigen moiety causes immediate visible clumping in the presence of SARS-CoV-2-specific AB, *e.g.*, in COVID-19 patients or vaccinated individuals (left panel). S-tag, twin-strep tag used for affinity purification of Nanospike. No visible agglutination occurs in the absence of antibodies (right panel). (c) ABO and Rh blood group identification *via* antibody-mediated agglutination. Blood samples of both AB+ and O+ groups exhibit no agglutination in the absence of antibodies. Visible agglutination is observed when the AB+ blood sample is mixed with antibody-A, antibody-B, and antibody-D, confirming the presence of antigen-A, antigen-B, and the Rhesus factor, respectively, on the RBC surface (top row). Conversely, the blood sample from the O+ group does not agglutinate when mixed with antibody-A or antibody-B, indicating the absence of these corresponding antigens. However, visible agglutination occurs with antibody-D, confirming the presence of the Rhesus factor (bottom row).

user can take a picture of the agglutinated sample, and the developed code can be used to interpret the result.

2.6 Image acquisition and classification algorithm

All images were collected using a mobile phone (iPhone 14 Pro, Apple Inc). Upon collection, the images were cropped and resized to a standardized resolution to ensure uniformity across the dataset. Additionally, each image was manually labeled based on the antibody concentration levels. Table 2 shows the categories of the dataset for binary analysis. First, a total of 180 images were classified into four levels (negative, weak, moderate, and strong) depending on the AB concentrations. To perform binary classification, these four categories were then put under two major classes named negative and positive, depending on the presence or absence of SARS-CoV-2 ABs in blood samples. The final dataset contained these two major classes and was saved as a CSV file. The class negative consisted of data from the negative category, as no agglutination occurred for these samples due to the absence of ABs in the blood. Conversely, the class positive included data from the strong, moderate, and weak categories since they produced different agglutination levels according to their respective concentration.

To eliminate the variation caused by visual interpretation, we applied a supervised machine-learning model, support vector machine (SVM), to distinguish between different sample categories. SVM is a suitable algorithm for binary classification that provides fast prediction and requires less computing power. We developed an SVM classifier using Python code. The dataset (CSV file) consisted of file paths, labels, and dataset split indicators. A label encoder was used to facilitate machine-learning model compatibility. Class names were defined based on the

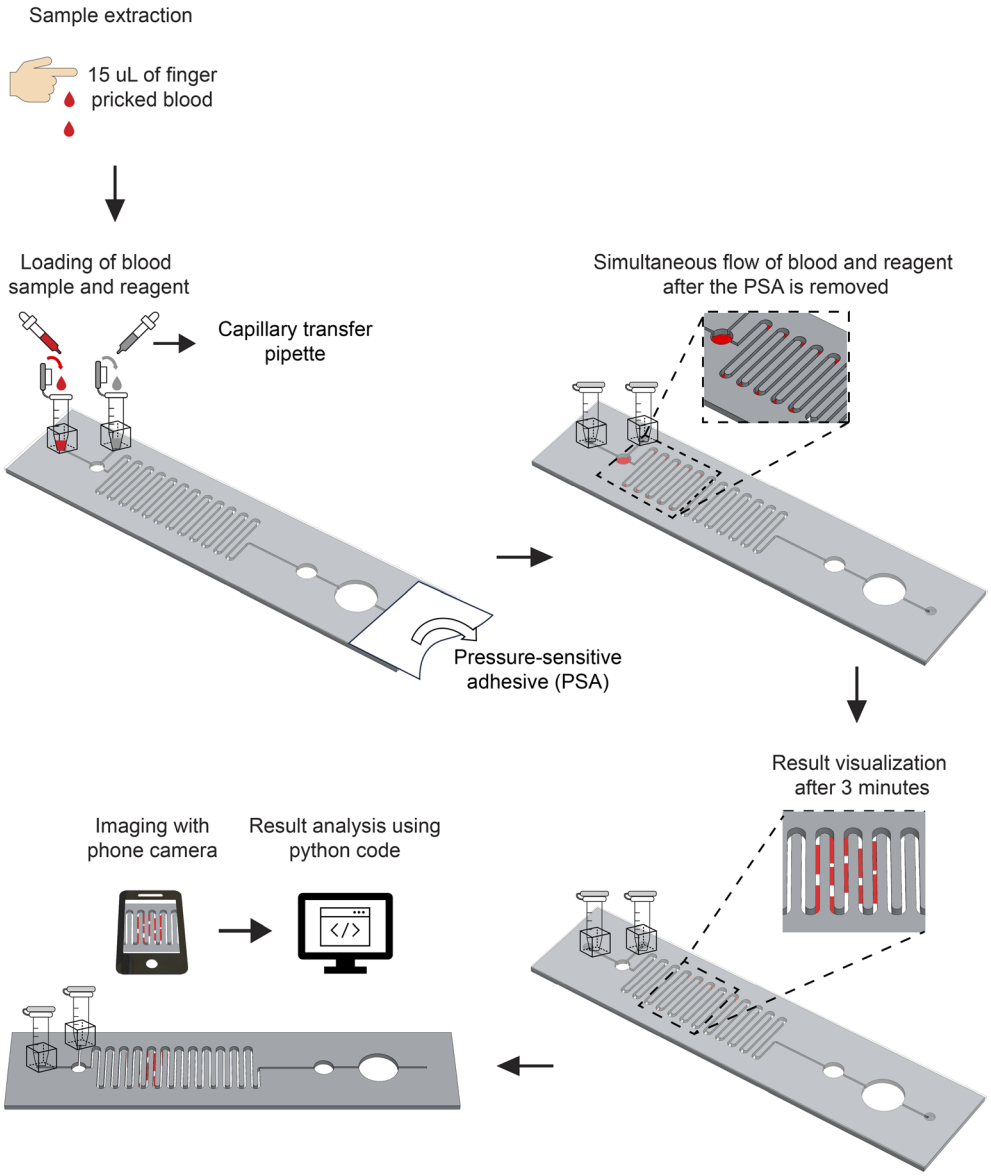

Fig. 3 On-chip hemagglutination assay. 15 μL of finger-pricked blood is collected using a capillary. The blood sample and the reagent are loaded into the inlets using capillaries. After loading, the caps of the tubes are closed, and the pressure-sensitive adhesive (PSA) is removed (direction indicated by the white arrow) off the vent. Upon removal of the PSA, the blood and the reagent flow simultaneously through the serpentine channels. The designed geometry ensures mixing of both fluids. After 3 minutes, results (agglutination or no agglutination, depending on the presence of ABs) can be observed in the channel. Apart from visual interpretation, a digital readout of the assay results can be achieved by taking pictures of the result with a phone camera and analyzing them using the developed machine-learning-based classifier model.

label encoder classes, providing meaningful representations for analysis. The dataset was then split into training (82 images) and testing (76 images) sets to train and assess the SVM model.

Table 2 Antibody (AB) concentration categories for binary classification

Class	Category	AB concentration (μg mL^{-1})
Negative	Negative	0
Positive	Weak	10
	Moderate	30
	Strong	60

Images were loaded and preprocessed from the dataset using the OpenCV library. We used a "load_and_preprocess_image" function to read the images, resize them to 256 × 256 pixels, and return the processed images. This function was applied to each image in the training and testing sets, and it stored the resized images along with their labels. After that, the code initialized a SVM classifier with a linear kernel. Next, the classifier was trained on the flattened training data. The model's accuracy was evaluated on both the training and testing sets, providing insights into potential overfitting issues. The code also generated a confusion matrix and a receiver operating characteristic (ROC) curve for binary classification. Finally, random images were used to evaluate and validate the model's

performance. We also extended the application of the classifier and performed a multi-level classification.

3 Results and discussion

3.1 Fluid pumping and mixing

To evaluate fluid flow and mixing within the device, we introduced food dyes, with yellow dye in one inlet and blue dye in the other. Upon cap closure and removal of the PSA from the vent, fluid flow commenced from both inlets. The initial velocity was high during the first three seconds, driven by pressurization from the cap closure. Following this, the flow decelerated and eventually ceased. Complete mixing of the fluids occurred within 3 to 4 seconds. The average velocity of the dye mixture during the first three seconds was approximately 45.7 mm s^{-1}. Using eqn. (1) and (2), we calculated the velocity and Reynolds number for the blood sample as 13.1 mm s^{-1} and 0.96, respectively.

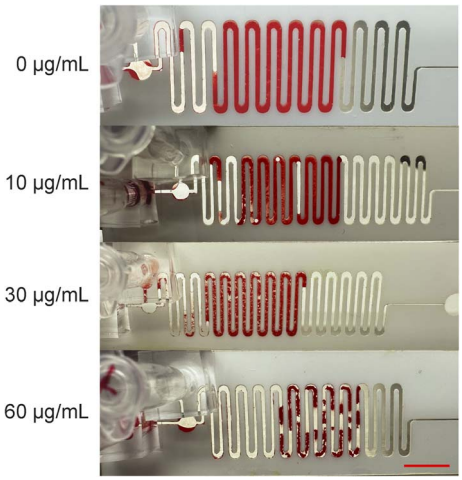

Fig. 4 Varying antibody concentrations lead to different levels of agglutination. Without antibody (0 μg mL^{-1}), no agglutination is observed, which is indicated by the continuous stream of blood with zero clumps and empty space within the start and end point of the flow. The number of clumps increases with the increase in antibody concentration. The highest antibody concentration, 60 μg mL^{-1}, depicts the strongest agglutination reaction, indicated by a greater number of clumps and empty spaces compared to the other cases. Scale bar in red = 2 mm.

$$\frac{v_{blood}}{v_{water}} = \frac{\mu_{water}}{\mu_{blood}} \quad (1)$$

v_{blood} = velocity of blood, v_{water} = velocity of water (0.04573 m s^{-1}), μ_{water} = viscosity of water (0.001 Pa − s @20 °C), μ_{blood} = viscosity of blood (0.0035 Pa − s @20 °C).

$$Re_{blood} = \frac{\rho_{blood} v_{blood} D_h}{\mu_{blood}} \quad (2)$$

ρ_{blood} = density of blood (1060 kg m^{-3}), v_{blood} = velocity of blood (0.01307 m s^{-1}), D_h = hydraulic diamater (0.000243 mm).

3.2 SARS-CoV-2 antibody detection and blood grouping

Fig. 4 illustrates varying levels of agglutination based on the different concentrations of antibodies in the blood sample. The level 0 μg mL^{-1} indicates blood samples with no antibody present, which we refer to as negative samples. The other three concentration levels were produced by spiking the negative blood samples with various concentrations of SCV-2 antibodies. No agglutination is observed for the negative blood sample (0 μg mL^{-1}). The agglutination reaction strength increases with an increase in antibody concentration. The strength of reactions

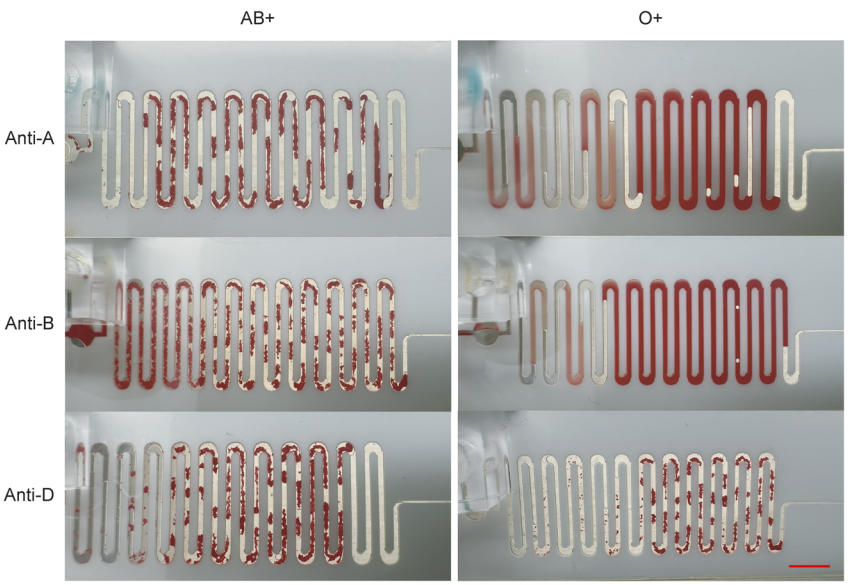

Fig. 5 On-chip blood grouping. The left panels indicate blood group AB due to agglutination with anti-A and anti-B reagents. The right panels indicate blood group O since no agglutination is observed with either anti-A or anti-B test serum. Agglutination with anti-D indicates positive Rh factors for both blood samples, confirming the blood groups to be AB+ and O+, respectively. Anti-A, anti-B, and anti-D are antibodies against antigens A, B, and D found on the surface of the red blood cells. Scale bar in red = 2 mm.

Table 3 Comparison of performance metrics for the proposed microfluidic platform against other reported systems

Metric	This work	Redecke *et al.*[16]	Nam *et al.*[8]	Sklavounos *et al.*[26]
Sample type	Whole EDTA blood	Whole EDTA blood or serum mixed with washed type-O RBCs	Whole blood with anti-A or anti-B antibodies	Whole blood
Sample volume	15 μL	Whole blood: 10–20 μL; serum: 5–10 μL	50 μL	<4 μL
Device workflow: Manual steps	Sample and reagent loading, cap closure, tape removal	Sample and reagent loading, mixing with a stick, card swivel	Sample and reagent loading, flow rate control by hand pipetting, alignment of microtrap chip to 3D printed aperture	Sample loading and process initiation
Device workflow: Automated steps	On-chip fluidic operations (pumping and mixing)	—	—	Reagent reconstitution, droplet operations, washing, transport, and imaging
Readout method	Visual and/or machine learning	Visual and/or machine learning	Absorbance-based	Automated image analysis
Sample-to-result time	≤3 minutes	≤3 minutes	Not reported	<6 minutes
Instrument requirement	Microfluidic chip, a smartphone (optional)	Hemagglutination test card, a smartphone	3D-printed microtrap chip, 3D printed aperture and microplate reader	Digital microfluidic instrument, droplet control system, pump, webcam and a laptop/computer
Platform cost (USD)	~$0.40 per cartridge	Not reported	Not reported	<$5000 (instrument)

can be visually differentiated by looking at the features of the agglutinated samples. For example, a strong reaction (60 μg mL^{-1} in Fig. 4) yields a greater number of clumps. These clumps are short, and there are greater areas of empty space along the path of the fluid from the beginning to the end than in other reactions with lower agglutination strength. As the concentration of ABs decreases, the agglutination of RBCs is reduced, correlating with a lower reaction strength.

We also performed on-chip blood grouping (Fig. 5). We tested samples of two blood groups, AB+ and O+. As expected, AB+ blood samples react with anti-A, anti-B, and anti-D reagents, producing readily visible agglutination. On the other hand, blood samples with the O+ blood group agglutinate only when reacting with the anti-D reagent. No agglutination is observed for anti-A and anti-B reagents, indicating the blood group does not have any A or B antigens on the red blood cells.

A comparison of key performance metrics across relevant hemagglutination-based studies is presented in Table 3. As shown in the table, our system simplifies user interventions, automates critical operational steps, and provides rapid sample-to-result times at a comparatively low per-cartridge cost, making it suitable to be applied in low-resource, PoC settings.

3.3 Data analysis

Although the simplicity of the hemagglutination test allows users to interpret results visually, we developed a support vector machine (SVM) classifier to assess the potential for integrating machine learning tools into the data analysis workflow. The performance of the classifier was validated using unseen datasets, evaluating its capacity for binary and multi-level classification. Furthermore, comparative analyses were conducted to assess how predictions from human evaluators and the machine learning model aligned with the actual sample categories. We also assessed prediction accuracy across different samples and investigated the variability in human interpretation. Fig. 6 represents an overview of the assessment of the SVM model and human interpretation.

The SVM model was trained on flattened image data to conform to the input structure required by the classifier. The dataset contained labeled images categorized as either class 0 (negative) or class 1 (positive). Fig. 6a shows the class distribution plot, confirming that the dataset was reasonably balanced, thus mitigating concerns about class imbalance and its potential effects on the classifier's performance. The model achieved perfect accuracy (1.00) during training, indicating its ability to capture the underlying patterns in the training data. However, when evaluated on a test set, accuracy dropped to 0.84. This discrepancy between training and test performance suggests the possibility of overfitting, where the model exhibits high performance on the training set but generalizes less effectively to unseen data. To further assess the model's generalization ability, we applied five-fold cross-validation, which yielded an average accuracy of 0.82. This result, closely aligned with the test set accuracy of 0.84, suggests that the model's internal validation was appropriate and its potential to generalize was reasonable. The binary classification

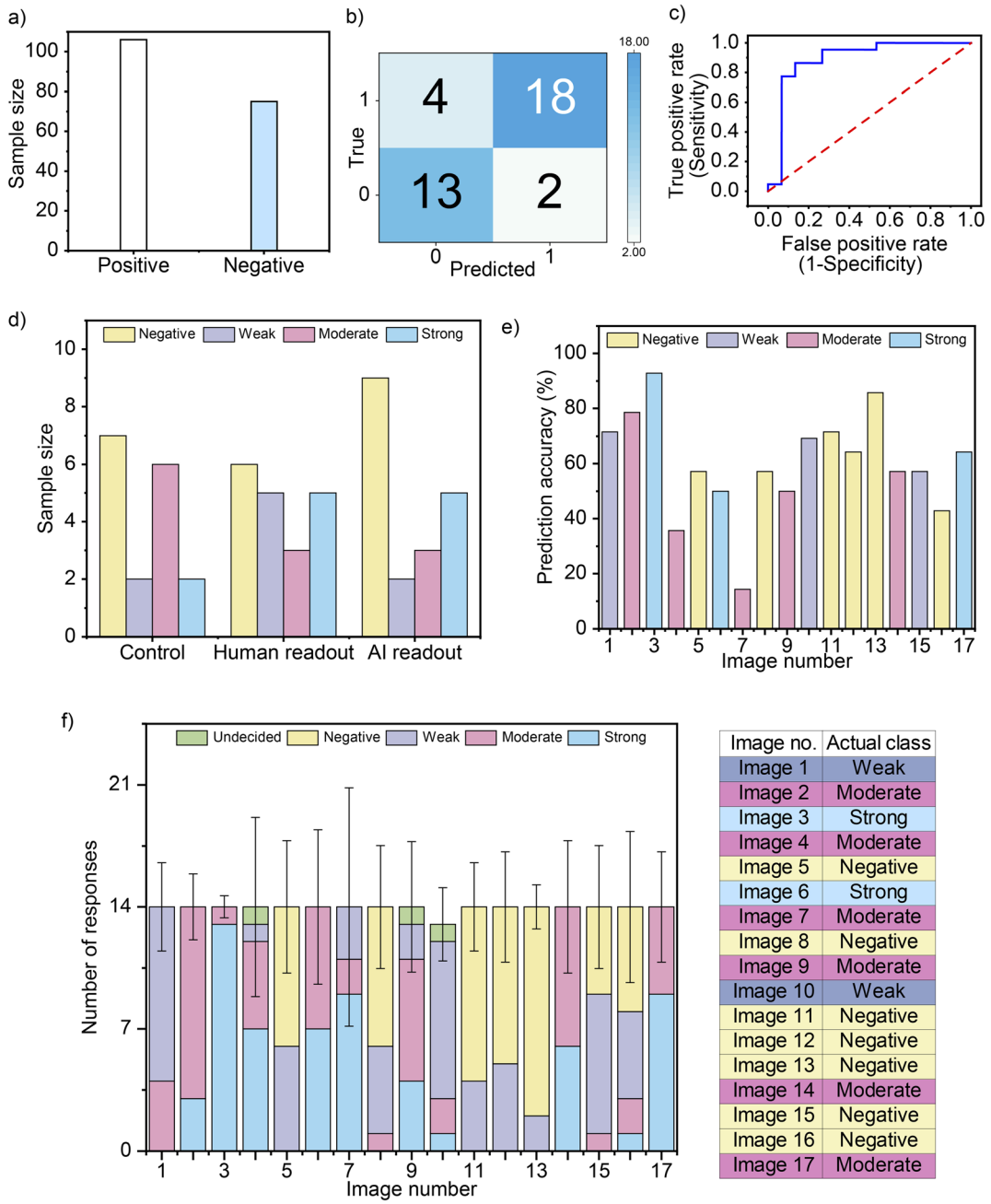

Image no.	Actual class
Image 1	Weak
Image 2	Moderate
Image 3	Strong
Image 4	Moderate
Image 5	Negative
Image 6	Strong
Image 7	Moderate
Image 8	Negative
Image 9	Moderate
Image 10	Weak
Image 11	Negative
Image 12	Negative
Image 13	Negative
Image 14	Moderate
Image 15	Negative
Image 16	Negative
Image 17	Moderate

Fig. 6 Performance of the SVM model and human in diagnostic evaluations. (a) Allocation of sample images between positive (106 images) and negative (75 images) classes used for training and testing the SVM classifier. (b) Confusion matrix showing the SVM model's capability to classify positive (agglutinated) and negative (non-agglutinated) samples in the test dataset ($n = 37$). The labels '0' and '1' refer to 'negative' and 'positive' classes. The model accurately identified 18 out of 22 positive and 13 out of 15 negative samples, with 4 false negatives and 2 false positives. (c) The receiving operating characteristics (ROC) curve demonstrating the classifier's performance at different classification thresholds. The dotted red line represents a reference line for area under the curve (AUC) = 0.5. (d) Comparison of the number of samples predicted by humans and AI to the number of samples with known AB concentration levels (control). (e) Prediction accuracy of human readouts for each of the sample images. (f) Response variation per image with standard deviation shown in error bars. The table represents the corresponding category of all the images under the actual class column. The classes have been assigned to each of the images depending on their concentration levels.

performance was assessed based on several standard metrics. The confusion matrix (Fig. 6b) indicated that the model correctly classified 13 out of 15 instances of the negative and 18 out of 22 instances of the positive classes, with four false negatives and two false positives. This suggests a decent overall performance in distinguishing between the two classes, especially considering the limited training data. Table 4 presents a classification report detailing precision, recall, and F1-scores for both classes. The model achieved a precision of 0.90 for class 1, indicating that 90% of the instances predicted as

Table 4 Classification report of the SVM classifier

	Precision	Recall	F1-score
Positive (class 1)	0.90	0.82	0.86
Negative (class 0)	0.76	0.87	0.81
Accuracy	0.84	0.84	0.84

Table 5 Summary of the chi-squared test

	Human interpretation	SVM classification
Chi-squared value (χ^2)	6.64	8.24
Degree of freedom (df)	3	3
p-value	0.08	0.04

positive were correctly classified. For class 0, the recall was 0.87, reflecting the model's ability to identify most true negative cases. The F1-score, a harmonic mean of precision and recall, was 0.86 for class 1 and 0.81 for class 0, demonstrating balanced performance in minimizing both false positives and false negatives. The overall classification accuracy is 0.84.

Fig. 6c presents a receiver operating characteristic (ROC) curve and its corresponding area under the curve (AUC) score of 0.89, further validating the model's predictive performance. An AUC score of 0.89 indicates a high probability that the model will correctly rank a randomly selected positive instance more than a randomly selected negative instance. Also, the ROC curve's trajectory signifies a favorable trade-off between the true positive rate (TPR) and the false positive rate (FPR), affirming the model's effectiveness across different decision thresholds. This indicates a well-calibrated model capable of adapting its threshold to balance sensitivity (TPR) and specificity (1 – FPR) based on the requirements of specific applications. To evaluate the model's potential in practical applications, we tested the SVM classifier on a newly acquired set of images that were not included in the original training or test datasets. The model achieved an accuracy of 94% on this independent dataset.

In addition to binary classification, we extended our investigation to multi-level classification, where the SVM classifier was tasked with distinguishing between multiple antibody concentration levels (*e.g.*, "negative," "weak," "moderate," "strong"). When tested on the same independent dataset as the binary classification, the performance of the multi-level model dropped notably, achieving an accuracy of 53%. While the classifier correctly identified all negative samples, most errors occurred in cases where images from adjacent classes, particularly "strong" *versus* "moderate" or "weak" *versus* "moderate" exhibited subtle visual differences. This indicates that the model's feature extraction capabilities were inadequate for capturing fine distinctions between closely related classes.

To assess the applicability of our proof-of-concept machine learning model within the diagnostic platform, we compared the classification performance of the SVM algorithm with human interpretation. A survey involving 14 participants was conducted using the same set of 17 images previously employed for evaluating the SVM model, ensuring that these images were distinct from those in the original training dataset. Fig. 6d compares human and SVM-based classifications against clinical samples with established antibody (AB) concentrations. The distribution of clinical samples within the control group included seven negative samples (0 μg mL^{-1} AB), two weak samples (10 μg mL^{-1} AB), six moderate samples (30 μg mL^{-1} AB), and two strong samples (60 μg mL^{-1} AB). Both human participants and the SVM model performed effectively in distinguishing positive from negative samples, as these categories exhibited clearly discernible differences in agglutination features. However, classification accuracy notably decreased for multi-level categorization tasks, with both humans and the machine learning model experiencing challenges when differentiating among weak, moderate, and strong samples. These difficulties arose due to subtle feature variations within intermediate categories. For example, both humans and the SVM model misclassified three out of six samples (50%) in the moderate (30 μg mL^{-1} AB) category. Furthermore, there is potential for misclassification from adjacent categories (weak or strong) being incorrectly labeled as moderate, underscoring the inherent complexity of multi-level classification. We anticipate that expanding the training dataset could enhance the performance of the machine learning model. To further investigate the nature of human classification errors and interpretive variations, we analyzed participant responses relative to the known sample categories (Fig. 6e). Additionally, we evaluated the variation in classifications across all 14 participants for each sample to identify trends in misclassification and disagreement (Fig. 6f). As shown in Fig. 6e, participants achieved at least 50% accuracy when identifying negative, weak, and strong samples but frequently misclassified moderate samples, often confusing them with adjacent categories. Fig. 6f presents the variability in participant responses per image, with standard deviations (indicated by error bars) reflecting the degree of disagreement among participants. Notably, the large standard deviations for moderate samples highlight the difficulty humans face in accurately distinguishing intermediate antibody concentration.

To assess whether the observed difference in multi-level classification accuracy between the SVM classifier and human evaluators was statistically significant, we conducted a chi-square test. The test compared the prediction outcomes of the AI model and human participants across all classification levels (negative, weak, moderate, and strong). The results of the test are summarized in Table 5. The chi-square test results yielded a *p*-value of 0.04 (<0.05) for the SVM classifier and 0.08 (>0.05) for the human interpretation. The *p*-value of the SVM classifier suggests that the classifier's interpretations were not due to chance; it statistically outperformed human participants in making accurate predictions. These results emphasize the potential application of the SVM classifier to perform multi-level classifications and improve clinical-level interpretations where humans may struggle with subtle distinctions.

4 Conclusion

We present a disposable microfluidic device to conduct hemagglutination assays. To demonstrate the versatility of our

device, we present its successful application in two distinct serological systems: rapid, low input detection of antibodies to SARS-CoV-2 and ABO blood typing. The device utilizes a pressure-driven passive pumping technique to mix reagents with a small blood sample, providing results within three minutes. Our developed microfluidic chip uses 15 μL of capillary blood and can detect both the absence and presence of antibodies, up to a concentration of 60 μg mL^{-1} in the user's blood. We also demonstrated the broader scope of the functionality and applicability of our developed microfluidic chip by performing on-chip blood typing that provides a clear yes/no answer. We also showed that our device can be integrated with machine learning models, such as SVM classification models, to enhance diagnostic accuracy. The SVM model achieved 94% accuracy in classifying binary (positive *versus* negative) agglutinations and 53% accuracy in classifying multi-level agglutinations. We compared the performance of the SVM classifier and humans in interpreting the results and conducted a chi-squared test to confirm whether the variability was random. The test confirmed that the SVM's predictions for multi-level classifications were statistically significant, while human predictions showed randomness. Considering that our SVM model was trained, tested and evaluated on only 180 samples, the *p*-value less than 5% statistical significance shows promise. Also, as future work, more advanced feature extraction techniques, such as deep learning or convolutional neural networks (CNNs), can be implemented for better accuracy. Likewise, the inclusion of positive control samples for the calibration of test results may enable more quantitative assessments of antibody concentrations.

Author contributions

Conceptualization: VR, HH, BG; investigation: MJ, ATA; methodology: MJ, BG; resources: RW, VR, HH; software: ATA, MJ; supervision: BG; writing – original draft: MJ, ATA; writing – review & editing: MJ, BG, VR, HH.

Conflicts of interest

The authors disclose that Rian Wendling, Vanessa Redecke, and Hans Häcker have current or former affiliations with NanoSpot.ai, which provided funding, reagents, and clinical samples utilized in this research. The remaining authors declare no competing interests.

Data availability

The data supporting the findings presented in the article have been included as part of the original manuscript. The code and dataset for Support Vector Machine can be found at **https://github.com/Munawar-Jawad/SARS-CoV-2-AB-Detection** with [Munawar-Jawad. (2025). MunawarJawad/SARS-CoV-2-AB-Detection: SARS-CoV-2 AB Detection (Dataset). Zenodo **https://doi.org/10.5281/zenodo.16112801**]. The Python code was written using Microsoft Visual Studio, which can be downloaded from **https://code.visualstudio.com/download**.

Supplementary information is available. See DOI: **https://doi.org/10.1039/d5ra05719a**.

Acknowledgements

The authors gratefully acknowledge financial support from NanoSpot.ai throughout this research. We would also like to express our sincere gratitude to Erik Kish-Trier for invaluable assistance with data collection and critical insights.

References

1 S.-M. Yang, S. Lv, W. Zhang and Y. Cui, Microfluidic Point-of-Care (POC) Devices in Early Diagnosis: A Review of Opportunities and Challenges, *Sensors*, 2022, **22**(4), 1620, DOI: **10.3390/s22041620**.

2 Y. Shen, T. Bin Anwar and A. Mulchandani, Current status, advances, challenges and perspectives on biosensors for COVID-19 diagnosis in resource-limited settings, *Sens. Acutators Rep.*, 2021, **3**, 100025, DOI: **10.1016/j.snr.2021.100025**.

3 T. R. Kozel and A. R. Burnham-Marusich, Point-of-Care Testing for Infectious Diseases: Past, Present, and Future, *J. Clin. Microbiol.*, 2017, **55**(8), 2313–2320, DOI: **10.1128/JCM.00476-17**.

4 E. Valera, *et al.*, COVID-19 Point-of-Care Diagnostics: Present and Future, *ACS Nano*, 2021, **15**(5), 7899–7906, DOI: **10.1021/acsnano.1c02981**.

5 N. Tazin, D. Patel, C. J. Lambert, M. H. M. Shad, J. Campbell and B. K. Gale, Automated passive serial dilution microfluidic chip for calcium quantification based on the Arsenazo III method, *Sens. Diagn.*, 2022, **1**(4), 810–820, DOI: **10.1039/D2SD00022A**.

6 B. Flower, *et al.*, Clinical and laboratory evaluation of SARS-CoV-2 lateral flow assays for use in a national COVID-19 seroprevalence survey, *Thorax*, 2020, **75**(12), 1082–1088, DOI: **10.1136/thoraxjnl-2020-215732**.

7 M. Lisboa Bastos, *et al.*, Diagnostic accuracy of serological tests for covid-19: systematic review and meta-analysis, *BMJ*, 2020, **370**(8256), m2516, DOI: **10.1136/bmj.m2516**.

8 S.-W. Nam, D.-G. Jeon, Y.-R. Yoon, G. H. Lee, Y. Chang and D. Il Won, Hemagglutination Assay via Optical Density Characterization in 3D Microtrap Chips, *Biosensors (Basel)*, 2023, **13**(7), 733, DOI: **10.3390/bios13070733**.

9 B. Xu, *et al.*, High-performance blood plasma separation based on a Janus membrane technique and RBC agglutination reaction, *Lab Chip*, 2022, **22**(22), 4382–4392, DOI: **10.1039/D2LC00508E**.

10 R. L. Kruse, *et al.*, A rapid, point-of-care red blood cell agglutination assay detecting antibodies against SARS-CoV-2, *Biochem. Biophys. Res. Commun.*, 2021, **553**, 165–171, DOI: **10.1016/J.BBRC.2021.03.016**.

11 S. Min, T. Zhan, Y. Lu, D. Pan, X. Chen and B. Xu, Rapid and easily identifiable blood typing on microfluidic cotton thread-based analytical devices, *Lab Chip*, 2023, **23**(21), 4680–4689, DOI: **10.1039/D3LC00501A**.

12 A. Townsend, *et al.*, A haemagglutination test for rapid detection of antibodies to SARS-CoV-2, *Nat. Commun.*, 2021, **12**(1), 1951, DOI: 10.1038/s41467-021-22045-y.
13 J. Qu, M. Chenier, Y. Zhang and C. Xu, A Microflow Cytometry-Based Agglutination Immunoassay for Point-of-Care Quantitative Detection of SARS-CoV-2 IgM and IgG, *Micromachines (Basel)*, 2021, **12**(4), 433, DOI: 10.3390/mi12040433.
14 C. J. Potter, Y. Hu, Z. Xiong, J. Wang and E. McLeod, Point-of-care SARS-CoV-2 sensing using lens-free imaging and a deep learning-assisted quantitative agglutination assay, *Lab Chip*, 2022, **22**(19), 3744–3754, DOI: 10.1039/D2LC00289B.
15 R. L. Kruse, *et al.*, A Hemagglutination-Based Semiquantitative Test for Point-of-Care Determination of SARS-CoV-2 Antibody Levels, *J. Clin. Microbiol.*, 2021, **59**(12), DOI: 10.1128/JCM.01186-21.
16 V. Redecke, *et al.*, A rapid and affordable point of care test for antibodies against SARS-CoV-2 based on hemagglutination and artificial intelligence interpretation, *Sci. Rep.*, 2021, **11**(1), 24507, DOI: 10.1038/s41598-021-04298-1.
17 I. Jang, H. Kang, S. Song, D. S. Dandy, B. J. Geiss and C. S. Henry, Flow control in a laminate capillary-driven microfluidic device, *Analyst*, 2021, **146**(6), 1932–1939, DOI: 10.1039/D0AN02279A.
18 S. YD and S. C. Maroo, Origin of Surface-Driven Passive Liquid Flows, *Langmuir*, 2016, **32**(34), 8593–8597, DOI: 10.1021/acs.langmuir.6b02117.
19 X. Xiang, *et al.*, Quantitative detection of aflatoxin B1 using quantum dots-based immunoassay in a recyclable gravity-driven microfluidic chip, *Biosens BioelectronOct*, 2021, **190**, 113394, DOI: 10.1016/j.bios.2021.113394.
20 C.-H. Chuang and Y.-Y. Chiang, Bio-O-Pump: a novel portable microfluidic device driven by osmotic pressure, *Sens. Actuators, B*, 2019, **284**, 736–743, DOI: 10.1016/j.snb.2019.01.020.
21 W. Qi, *et al.*, A finger-actuated microfluidic biosensor for colorimetric detection of foodborne pathogens, *Food Chem.*, 2022, **381**, 131801, DOI: 10.1016/j.foodchem.2021.131801.
22 C. K. Byun, K. Abi-Samra, Y. Cho and S. Takayama, Pumps for microfluidic cell culture, *Electrophoresis*, 2014, **35**(2–3), 245–257, DOI: 10.1002/elps.201300205.
23 A. P. Iakovlev, A. S. Erofeev, and P. V. Gorelkin, *Novel Pumping Methods for Microfluidic Devices: A Comprehensive Review*, MDPI, 2022, DOI: 10.3390/bios12110956.
24 V. Narayanamurthy, *et al.*, Advances in passively driven microfluidics and lab-on-chip devices: a comprehensive literature review and patent analysis, *RSC Adv.*, 2020, **10**(20), 11652–11680, DOI: 10.1039/D0RA00263A.
25 M. Boyd-Moss, S. Baratchi, M. Di Venere and K. Khoshmanesh, Self-contained microfluidic systems: a review, *Lab Chip*, 2016, **16**(17), 3177–3192, DOI: 10.1039/C6LC00712K.
26 A. A. Sklavounos, *et al.*, Digital Microfluidic Hemagglutination Assays for Blood Typing, Donor Compatibility Testing, and Hematocrit Analysis, *Clin. Chem.*, 2021, **67**(12), 1699–1708, DOI: 10.1093/CLINCHEM/HVAB180.